Original Article

Journal of Tissue Engineering
Volume 16: 1–19
© The Author(s) 2025
Article reuse guidelines:
sagepub.com/journals-permissions
DOI: 10.1177/20417314241295928
journals.sagepub.com/home/tej
Sage

Insulin resistance compromises midbrain organoid neuronal activity and metabolic efficiency predisposing to Parkinson's disease pathology

Alise Zagare[1], Janis Kurlovics[2], Catarina Almeida[1,3], Daniele Ferrante[1], Daniela Frangenberg[1], Armelle Vitali[4], Gemma Gomez-Giro[1], Christian Jäger[5], Paul Antony[6], Rashi Halder[7], Rejko Krüger[4,8], Enrico Glaab[9], Egils Stalidzans[2], Giuseppe Arena[4] and Jens C Schwamborn[1]

Abstract

Growing evidence indicates that type 2 diabetes (T2D) is associated with an increased risk of developing Parkinson's disease (PD) through shared disease mechanisms. Studies show that insulin resistance, which is the driving pathophysiological mechanism of T2D plays a major role in neurodegeneration by impairing neuronal functionality, metabolism and survival. To investigate insulin resistance caused pathological changes in the human midbrain, which could predispose a healthy midbrain to PD development, we exposed iPSC-derived human midbrain organoids from healthy individuals to either high insulin concentration, promoting insulin resistance, or to more physiological insulin concentration restoring insulin signalling function. We combined experimental methods with metabolic modelling to identify the most insulin resistance-dependent pathogenic processes. We demonstrate that insulin resistance compromises organoid metabolic efficiency, leading to increased levels of oxidative stress. Additionally, insulin-resistant midbrain organoids showed decreased neuronal activity and reduced amount of dopaminergic neurons, highlighting insulin resistance as a significant target in PD prevention.

Keywords

Organoids, brain organoids, Parkinsons disease, diabetes, metabolism

Date received: 14 May 2024; accepted: 15 October 2024

---

[1]Developmental and Cellular Biology, Luxembourg Centre for Systems Biomedicine (LCSB), University of Luxembourg, Esch-sur-Alzette, Luxembourg
[2]Bioinformatics Lab, Rīga Stradiņš University, Riga, Latvia
[3]Health Sciences Research Center, Faculty of Health Sciences Research, Faculty of Health Sciences, University of Beira Interior, Covilhã, Portugal
[4]Translational Neuroscience, Luxembourg Centre for Systems Biomedicine (LCSB), University of Luxembourg, Esch-sur-Alzette, Luxembourg
[5]Metabolomics Platform, Luxembourg Centre for Systems Biomedicine (LCSB), University of Luxembourg, Esch-sur-Alzette, Luxembourg
[6]Bioimaging Platform, Luxembourg Centre for Systems Biomedicine (LCSB), University of Luxembourg, Esch-sur-Alzette, Luxembourg
[7]Sequencing Platform, Luxembourg Centre for Systems Biomedicine (LCSB), University of Luxembourg, Esch-sur-Alzette, Luxembourg
[8]Transversal Translational Medicine, Luxembourg Institute of Health (LIH), Strassen, Luxembourg
[9]Biomedical Data Science, Luxembourg Centre for Systems Biomedicine (LCSB), University of Luxembourg, Esch-sur-Alzette, Luxembourg

Corresponding author:
Jens C Schwamborn, Developmental and Cellular Biology, Luxembourg Centre for Systems Biomedicine (LCSB), University of Luxembourg, 2, place de l'Université, Esch-sur-Alzette 4365, Luxembourg.
Email: jens.schwamborn@uni.lu

Introduction

Parkinson's disease (PD) is the second most frequent neurodegenerative disease, which affects the motor and cognitive function of patients due to the progressive degeneration of dopaminergic neurons in the *substantia nigra* region of the midbrain.[1,2] Most PD cases are idiopathic with an unknown genetic cause. Along with age as the primary risk factor, also environment, genetic risk factors and comorbidities contribute to the development of idiopathic PD.[2] Recent epidemiological studies and meta-analyses show that type 2 diabetes (T2D) is associated with a 30%–40% increased risk of developing PD.[3–5] It has also been shown that patients affected by PD and T2D comorbidity, suffer from more severe motor symptoms and cognitive decline.[6–9] Moreover, it has been suggested that T2D and PD share underlying pathophysiological mechanisms.[5,10,11] Along with the dysregulated energy metabolism, aberrant protein aggregation, accumulation of reactive oxygen species and inflammation, insulin resistance seems to play a pivotal role in converging most of these common mechanisms. Insulin receptor presence in the basal ganglia and *substantia nigra* of healthy brains, and their loss in PD patient brains, suggests the particular importance of insulin in the regulation of dopaminergic neuron survival, as well as in the maintenance of their functional and metabolic homeostasis.[12,13] In addition, there is evidence showing that insulin resistance can occur in PD patient brains independently of T2D, highlighting insulin resistance as a potential factor contributing to PD onset and progression.[13,14]

In this study, we aimed to evaluate insulin resistance-mediated effects on the healthy midbrain to investigate through which molecular mechanisms insulin resistance might favour PD onset and progression. In order to address this question, we used induced pluripotent stem cell (iPSC)-derived human midbrain organoids from healthy donors and exposed them to a high insulin concentration, which mimics hyperinsulinemia and promotes insulin resistance, or to a more physiological insulin concentration to retain cells in an insulin-sensitive state. Using a combination of computational and experimental methods we predicted and validated insulin resistance-dependent metabolic alterations and demonstrated that insulin-resistant midbrain organoids experience functional decline in terms of electrophysiological activity. Further, they produce less dopamine and have a reduced amount of dopaminergic neurons. Overall these results support the notion that insulin resistance is a considerable risk factor for PD and that it can be modelled *in vitro*.

Materials and methods

iPSC-derived dopaminergic neuron differentiation and characterisation

iPSC from a healthy donor were first converted into neuroepithelial stem cells (NESCs) based on the protocol previously described.[15] In brief, the N2B27 medium was used as the basis media for cell culture. N2B27 consists of DMEM-F12 (Cat. No. 21331046; Thermo Fisher Scientific) and Neurobasal (Cat. No. 10888022; Thermo Fisher Scientific) 50:50 and is supplemented with 1:200 N2 supplement (Cat. No. 17502001; Thermo Fisher Scientific), 1:100 B27 supplement w/o Vitamin A (Cat. No. 12587001; Life Technologies), 1% GlutaMAX (Cat. No. 35050061; Thermo Fisher Scientific) and 1% penicillin/streptomycin (Cat. No. 15140122; Thermo Fisher Scientific). N2B27 base media was supplemented with 3 µM CHIR-99021 (Cat. No. CT 99021; Axon Medchem), 0.75 µM purmorphamine (Cat. No. ALX-420-045; Enzo Life Science) and 150 µM ascorbic acid (Cat. No. A4544; Sigma). For the generation of midbrain-specific dopaminergic neurons, NESCs were seeded into Geltrex-coated wells in a differentiation medium consisting of N2B27 containing 1 µM PMA, 200 µM ascorbic acid, 10 ng/ml BDNF, 10 ng/ml GDNF, 1 ng/ml TGF-b3 and 500 µM dbcAMP. After 6 days, differentiating NESCs were shifted to the same medium but without PMA (replaced every 2 days) and kept until day 30.

The expression of neuronal differentiation markers was assessed by flow cytometry. Briefly, cells were detached with Accutase (Cat. No. A6964; Sigma) and then fixed in 4% PFA for 15 min. After three washes in fluorescence-activated cell sorting (FACS) buffer (PBS + 5% BSA + 0.1% Sodium Azide), cells were centrifuged at 700*g* for 5 min and the resulting cell pellet resuspended in Saponin buffer (PBS + 1% BSA + 0.05% Saponin). After 30 min of incubation at 4°C, cells were pelleted again and then resuspended in Saponin buffer containing the TH (Cat. No. AB152; Millipore) and Tuj1 (Cat. No. 801201; Biolegend) primary antibodies (1:100 dilution, 30 min at 4°C under shaking). Cells were washed three times in FACS buffer, and then incubated for 30 min with anti-mouse Alexa 488 (for TUJ1) and anti-rabbit Alexa 568 (for TH) secondary antibodies (at 4°C in the dark). After two washes in the FACS buffer, cells were pelleted and finally resuspended in PBS. Cells were analysed with the BD LSRFortessa flow cytometer and the mean fluorescence intensity of each dye was assessed on at least 10,000 single cells using the FlowJo software (v.10.7.2.).

Midbrain organoid culture

Cell lines used in this study are summarised in Table S1. As the starting population for midbrain organoid generation, we used NESCs described in Reinhardt et al.[15] NESCs were cultured as described in section 'iPSC-derived dopaminergic neuron differentiation and characterisation'. Midbrain organoids were generated as described in Monzel et al.[16] and Nickels et al.[17] For organoid generation, at 80% of confluency, NESCs were detached using Accutase (Cat. No. A6964; Sigma) and viable cells were counted using Trypan Blue. 9×10^5 cells were transferred into 15 ml of N2B27 maintenance media for seeding in 96-well ultra-low attachment plates (Cat. No. F202003; faCellitate). In each well 150 µl with 9000 cells were distributed. Plates were centrifuged at 300*g* for 1 min to facilitate colony formation at the bottom of the well. On the second day of organoid culture, media was changed to N2B27 pattering media, which is N2B27 base media supplemented with 10 ng/ml hBDNF (Cat. No. 450-02-1mg; Peprotech), 10 ng/ml hGDNF (Cat. No. 450-10-1mg; Peprotech), 500 µM dbcAMP (Cat. No. 100-0244; STEMCELL Technologies,), 200 µM ascorbic acid (Sigma), 1 ng/ml TGF-β3 (Cat. No. 100-36E; Peprotech) and 1 µM purmorphamine (Cat. No. ALX-420-045; Enzo Life Science). Media was next changed on the fifth day of organoid culture. On day 8 of organoid culture, organoids for high-content imaging were embedded in extracellular matrix-like Gelltrex (Cat. No. A1413302; Thermo Fisher Scientific) droplets as described in Zagare et al.,[18] to support the outgrowth of neurites. Embedded organoids were kept in dynamic conditions on an orbital shaker (IKA), rotating at 80 rpm until the collection day. From day 8 of organoid culture organoids were kept in N2B27 differentiation media which only differs from the pattering media by lack of purmorphamine. Media changes were done every 3–4 days for embedded and non-embedded organoids until the day of sample collection – day 30 or 60 of organoid culture. For organoid cultures with reduced insulin concentration in media, commercial N2 supplement was substituted by self-made N2 supplement w/o insulin starting from day 2 of organoid culture. Self-made N2 was prepared as described in Harrison et al.,[19] adding human Apo-transferrin (Cat. No. T1147; Sigma), Putrescine dihydrochloride powder, cell-culture tested (Cat. No. P5780; Sigma), Sodium selenite powder, cell-culture tested (Cat. No. S5261; Sigma), Progesterone powder, cell-culture tested (Cat. No. P8783; Sigma) in cell media in the same concentrations as in the commercial N2 supplement.

All cell cultures were tested for mycoplasma contamination once per month using LookOut® Mycoplasma PCR Detection Kit (Cat. No. MP0035-1KT; Sigma).

Insulin ELISA

Insulin in fresh cell culture media and organoid supernatant was measured with Insulin ELISA (Cat. No. 10-1113-01; Mercodia) following the manufacturer's instructions. The supernatant was collected after 2 h of incubation with cells. Before the essay media and supernatant were diluted in DMEM-F12 (Cat. No. 21331046; Thermo Fisher Scientific) 1:500 to ensure that insulin concentration do not exceed the measurement range of the kit. DMEM-F12 was used as a negative control for the assay as it does not contain any insulin. All samples were measured in duplicates from which the average was calculated.

Western Blot

iPSC-derived dopaminergic neurons were lysed in 1% SDS supplemented with protease inhibitors (Cat. No. 11697498001; Roche) and immediately boiled at 95°C for 5 min. Cell extracts were then sonicated at 4°C for five cycles (30 s on/30 s off) with the Bioruptor Pico (Diagenode), prior to proceeding with protein quantification using the Pierce™ BCA Protein Assay Kit (Cat. No. 23225; Thermo Fisher Scientific). Ten micrograms of proteins were resolved using SDS-PAGE (4%–12% Bis-Tris precast gels in buffer MES), followed by transfer on a nitrocellulose membrane in Tris-Glycine buffer containing 20% ethanol (1 h 15 at 400 mA). Membranes were blocked for 1 h in TBS buffer containing 0.2% Tween (TBS-T) and 5% BSA, and then incubated overnight at 4°C with the primary antibodies (see Table S2). Membranes were then washed in TBS-T for 30 min, followed by 1 h incubation at RT with the corresponding HRP-linked anti-rabbit or anti-mouse secondary antibodies. After additional washes in TBS-T for 30 min, proteins were revealed using the ECL prime and images acquired with the STELLA 8300 imaging system (Raytest).

For the analysis of midbrain organoids, eight non-embedded organoids were pooled together and lysed using RIPA buffer (Cat. No. ab156034; Abcam) supplemented with cOmplete™ Protease Inhibitor Cocktail (Cat. No. 11697498001; Roche,) and Phosphatase Inhibitor Cocktail Set V (Cat. No. 524629; Merck) for 20 minon ice. To disrupt DNA, protein lysates were sonicated for 10 cycles (30 s on/30 s off) using the Bioruptor Pico (Diagenode). Samples were centrifuged at 4°C for 30 min at 14,000*g*. Protein concentration was determined using the Pierce™ BCA Protein Assay Kit (Cat. No. 23225; Thermo Fisher Scientific). The concentration of samples was adjusted by dilution with RIPA buffer. Samples were then boiled at 95°C for 5 min in denaturalising loading buffer. Twenty micrograms of protein of each sample was used for protein detection. Proteins were separated using SDS polyacrylamide gel electrophoresis (Bolt™ 4%–12% Bis-Tris Plus Gel; Thermo Fisher Scientific) and further transferred onto a PVDF membrane (Thermo Fisher Scientific) using iBlot™ 2 Gel Transfer Device (Thermo Fisher Scientific). For IRS1 protein, protein separation was achieved using NuPAGE™ 3%–8%, Tris-Acetate gel (Thermo Fisher Scientific). After transfer, membranes were fixed in 0.4% paraformaldehyde (PFA) in PBS for 30 min at room temperature (RT) and then washed twice with PBS for 10 min. Membranes then were blocked for 1 h at RT in 5% skimmed milk powder or 5% BSA (for phosphorylated proteins) and 0.2% Tween in PBS following overnight incubation at 4°C with the primary antibodies prepared in 5% skimmed milk powder or 5% BSA (for phosphorylated proteins) and 0.2% Tween in PBS. A list of primary antibodies is provided in Table S2. After incubation with primary antibodies, membranes were washed three times for 5 min with 0.02% Tween in PBS and incubated for 1 h at RT with HRP-linked antibodies – anti-rabbit (Cat. No. NA934; VWR) or anti-mouse (Cat. No. NA931; VWR). Membranes were then washed three times for 10 min with 0.02% Tween in PBS. The signal was developed using a chemiluminescent substrate (Cat. No. 34580; Life Technologies,) and imaged with STELLA 8300 imaging system (Raytest). After developing phospho-AKT and phospho-FOXO1 protein signal, membranes were stripped using Restore™ Western Blot Stripping Buffer (Cat. No. 21063; Thermo Fisher Scientific) for 15 min at 37°C, and then washed twice for 10 min with 0.2% Tween in PBS at RT. Membranes were blocked again for one hour before overnight incubation with the AKT pan or FOXO1 pan antibody respectively.

Band intensity was quantified using ImageJ software. Phosphorylated protein relative abundance was determined in comparison to the total protein. For all other proteins, relative abundance was determined in comparison to the housekeeping protein β-Actin. Results were batch-normalised to the mean intensity of all samples. Experiment was repeated for three independent organoid generation rounds.

Extracellular metabolite detection with GC-MS

Spent medium pooled from five embedded organoids from each cell line and condition in triplicates were collected 72 h after the last media change. Extracellular metabolite extraction and subsequent GC-MS analysis were performed as previously described.[20]

Metabolite derivatisation was performed using a multipurpose sampler (Gerstel). Dried polar sample extracts were dissolved in 20 µl pyridine, containing 20 mg/ml of methoxyamine hydrochloride (Sigma-Aldrich), and incubated under shaking for 120 min at 45°C. After adding 20 µl *N*-methyl-*N*-trimethylsilyl-trifluoroacetamide (MSTFA; Macherey-Nagel), samples were incubated for an additional 30 min at 45°C under continuous shaking.

GC-MS analysis was performed using an Agilent 7890B GC – 5977A MS instrument (Agilent Technologies). A sample volume of 1 µl was injected into a Split/Splitless inlet, operating in split mode (10:1) at 270°C. The gas chromatograph was equipped with a 5 m guard column + 30 m (I.D. 250 µm, film 0.25 µm) DB-35MS capillary column (Agilent J&W GC Column). Helium was used as the carrier gas with a constant flow rate of 1.2 ml/min.

The GC oven temperature was held at 90°C for 1 min and increased to 270°C at 9°C/min. Then, the temperature was increased to 320°C at 25°C/min and held for 7 min. The total run time was 30 min. The transfer line temperature was set constantly to 280°C. The mass selective detector (MSD) was operating under electron ionisation at 70 eV. The MS source was held at 230°C and the quadrupole at 150°C. Mass spectrometric data were acquired in full scan mode (m/z 70–700).

All GC-MS chromatograms were processed using MetaboliteDetector (v3.2.20190704).[21] Compounds were annotated by retention index and mass spectrum using an in-house mass spectral library. The following deconvolution settings were applied: Peak threshold: 10; Minimum peak height: 10; Bins per scan: 10; Deconvolution width: 5 scans; No baseline adjustment; Minimum 15 peaks per spectrum; No minimum required base peak intensity. The dataset was normalised by using the response ratio of the integrated peak area of the analyte and the integrated peak area of the internal standard. Final metabolite relative abundance was normalised to the total area of organoids from each cell line and condition from the respective batch.

Multielectrode array

Multielectrode array (MEA) recordings were performed using the Maestro system from Axion BioSystems. Firing activity was recorded for midbrain organoids at day 30 and 60 of organoid culture from three independent organoid generations for both time points. Three days before recording non-embedded organoids were placed into CytoView MEA 48-Black (Cat. No. M768-tMEA-48B-5; Axion) plate precoated with 0.1 mg/ml poly-D-lysine hydrobromide (Cat. No. P7886; Sigma) for 24 h following 10 µg/ml laminin (Cat. No. L2020; Sigma) coating for another 24 h. Organoids were positioned at the centre of the well and covered with a droplet (20 µ) of Geltrex (Cat. No. A1413302; Invitrogen,) to secure organoid attachment. Recorded firing activity was exported using AxIS software (v.2.1. Axion) and analysed with R (version 4.2.2). The organoid activity was analysed from the active electrodes. Electrodes that did not record any activity or recorded less than three spikes in 5 min were excluded from the analysis. Outliers were excluded using the interquartile range (IQR) 1.5 method based on 25th and 75th percentiles. Data was batch normalised by the average value of the batch at each time point.

Local field-potential recording

Individual organoids were randomly selected from three different organoid generation batches and recorded between day 30 and 33 or day 60 and 63. For each organoid recordings were performed in multiple local fields. Each measurement is depicted as a separate data point. Live organoids were stuck on the bottom of the slice recording chamber using a customised platinum anchor and were perfused with a fast-flow rate (8–10 ml/min) warmed (37°C) extracellular solution containing (in mM): 140 NaCl, 2 $CaCl_2$, 1 $MgCl_2$, 4 KCl, 10 glucose, and 10 HEPES (pH 7.3 with NaOH), bubbled with an air pump at room atmospherically condition. Solution temperature was controlled by

Perfusion Temperature Controller (Scientifica). To avoid bubbles in the recording chamber, a bubble trap was employed in the inlet line, perfused by gravity drip. Local field-potential (LFP) activity was recorded using a patch pipette prepared from thin-borosilicate glass (1.5 mm OD, 0.84 mm ID; Cat. No. 1B150F-4; World Precision Instruments) pooled and fire-polished on a Flaming/Brown micropipette puller (Model P-1000; Sutter Instrument) to a final resistance of 1.5–2.5 MΩ when filled with standard extracellular solution. LFP recordings were performed with a Multiclamp 700B/Digidata1550 system (Molecular Devices) in a current-clamp configuration on a visually identified zone of healthy neurons on the organoid using a slice scope upright microscope (Scientifica). The patch pipette was pushed against the organoid for a depth of 40–60 μm until a small increase in the standard deviation of the recorded voltage was seen.

Data were acquired with Clampex software (v.11.2; Molecular Devices) at 3 kHz sample frequency and filtered at 3 kHz with a low-pass Bessel filter and 1 Hz with a high-pass filter. All data were analysed offline with Clampex software (v.11.2; Molecular Devices). The detection of LFP was done in 5-min temporary windows recording with the threshold search function that recognises only spikes over 6× standard deviation. Bursts with a minimum of 3 spikes and an inter-spike interval of ⩽150 ms were detected and considered for analysis.

Immunofluorescence staining for NESC characterisation

For immunofluorescence characterisation, NESCs were seeded on Geltrex-coated coverslips placed in a 24-well cell culture plate. At 60%–70% of confluency, NESCs were fixed for 15 min at RT with 4% paraformaldehyde (PFA). Then cells were washed three times for 5 min with PBS, which was followed by cell permeabilisation with 0.3% Triton X-100 in PBS for 15 min at RT. Afterwards, cells were washed three times for 5 min with PBS and then blocked with 10% fetal bovine serum (FBS) in PBS for 1 h at RT. Incubation with primary antibodies (Table S3) was done overnight at 4°C. Antibodies were diluted in 3% FBS in PBS. After overnight incubation, cells were washed three times for 5 min with PBS and incubated for 1 h at RT with Alexa Fluor® conjugated secondary antibodies (Table S3) and nuclei stain Hoechst 33342 (Cat. No. 62249; Invitrogen). After three washes for 5 min with PBS, coverslips were mounted on a glass slide for image acquisition.

Immunofluorescence staining of organoid sections

Organoids were fixed with 4% PFA for 6 h at RT and then washed three times with PBS for 15 min. Individual organoids were embedded in 3% low-melting point agarose (Cat. No. 840100; Biozym Scientific GmbH). Using a vibrating blade microtome (Leica VT1000s), organoids were sliced into 70 μm sections. Sections were permeabilised with 0.5% Triton X-100 for 30 min at RT and then blocked with blocking buffer (2.5% normal donkey serum, 2.5% BSA, 0.01% Triton X-100 and 0.1% sodium azide). Sections were incubated with primary antibodies diluted in a blocking buffer for 48 h at 4°C on an orbital shaker. Primary antibodies are listed in Table S3. After incubation with primary antibodies, sections were washed three times for 5 min with 0.01% Triton X-100 in PBS. Then sections were incubated with nuclei stain Hoechst 33342 (Cat. No. 62249; Invitrogen) in dilution of 1:10,000 and The Alexa Fluor® conjugated secondary antibodies (Table S3) for 2 hours at RT on an orbital shaker. Sections were washed twice for 5 min with 0.01% Triton X-100 in PBS and once with MiliQ. Sections were mounted on slides (Cat. No. BM-9244; De Beer Medicals) and covered with mounting media Fluoromount-G® (Cat. No.0100-01; SouthernBiotech).

Apoptotic cells were stained using Tunel In Situ Cell Death Detection Kit, Fluorescein (Cat. No. 11684795910; Merck). Kit components were integrated into the staining procedure. Staining with primary antibodies was done as described above. Secondary antibodies and Hoechst were diluted in the Tunel kit buffer. Sections were incubated for 1 h at RT on an orbital shaker followed by washing and mounting steps as described above.

Image acquisition and analysis

High-content imaging was performed using the Yokogawa CV8000 high-content screening microscope with a 20× objective. One to three sections from at least three independent organoid generation rounds were analysed per cell line and condition for each staining combination. Acquired images were analysed with a customised pipeline using Matlab (v.2021a) as described in Bolognin et al.[22] and Monzel et al.[23] Sections with non-optimal mask for a target protein or out of focus were excluded from further analysis. Data was batch normalised by the average value of the batch per feature and per time point. Outliers were excluded using the interquartile range (IQR) 1.5 method based on 25th and 75th percentiles. Qualitative images were acquired using a confocal laser scanning microscope (Zeiss LSM 710) with either a 20×, 40× or 60× objective and processed with Zen Software (Zeiss).

RNA sequencing and analysis

The total RNA was extracted from 12 embedded organoids, which were pooled from three independent organoid generations (four organoids from each generation per cell line and per condition). RNA isolation was achieved using Trizol reagent (Cat. No. 15596026; Thermo Fisher Scientific) following the manufacturer's protocol. Library preparation was done using TruSeq stranded mRNA library preparation kit (Cat. No. 20020594; Illumina) and sequenced on NextSeq2000. The raw RNA-seq data were pre-processed using the software package 'Rsubread' (version 1.34.7).[24]

Metabolic modelling

Gene expression from RNA sequencing was normalised to the transcripts per kilobase million (TPM) reads. The Median of TPM expression was calculated between the three cell lines per IR and IS condition to enable a generation of one context-specific model per condition. Gene EntrezID as required input in the modelling pipeline was mapped using the clusterProfiler package (version 3.9)[25] in R (version 3.6.2). Context-specific models were reconstructed from the stoichiometrically and flux-consistent subset of the human genome-scale metabolic network Recon3[26] using the rFASTCORMICS pipeline.[27] Additionally, models were constrained by the cell culture media composition, allowing uptake of only those metabolites present in the media. Models were analysed in Matlab (v.2019b) using the COBRA toolbox.[28]

Models were compared by reaction composition, using the *setdiff* function in Matlab. Reactions that were unique for one of the models, were assigned to a subsystem. Subsystems with more than eight reactions unique for one of the models were selected for further analysis. For selected subsystems, the number of unique reactions was expressed as a percentage of the total number of reactions in the respective subsystem in Recon3.

Flux of the ATP demand/generation 'DM_atp_c_ 'reaction in each model was estimated by the addition of quantitative constraints of glucose uptake 'EX_glc_D[e]', lactate secretion 'EX_lac_L[e]' and biomass reaction. Biomass increase per hour was calculated based on embeded organoid area increase between day 16 and 30 of organoid culture. Dry weight (DW) for a single cell was calculated considering that the total protein fraction within the dopaminergic neurons neurons is 55.93%.[29] Glucose uptake and lactate secretion were calculated as mmol/gDW*h. The concentration change of glucose and lactate within 72 h for DW was estimated by comparing the relative abundance determined with GC-MS to metabolite concentration in the commercial media. Glucose and lactate relative abundance for each model was calculated as a median between the samples, after averaging values between technical replicates. The lower and upper bound for glucose uptake and lactate secretion were set as ±10% of the calculated flux, while the lower and upper bound for biomass were kept exact. Next, estimated ATP demand for each model was used as an objective function set as the lower bound for the 'DM_atp_c_' reaction. Further, flux variability analysis (FVA) using IBM_CPLEX solver (version 12.10) was performed for shared reactions between the two models for the subsystems of interest – all subsystems determined to have the largest differences in reaction composition with the addition of glycolysis, TCA and OXPHOS. An average of min and max fluxes was calculated for visualisation of flux variability between the two models. ATP perturbations were performed by setting the upper bound of reactions of interest to 0 and re-estimating ATP demand flux.

Intracellular ATP assay

Intracellular ATP was measured using luminescence-based CellTiter-Glo® 3D Cell Viability Assay (Cat. No. G9681; Promega) following the manufacturer's instructions. Three organoids per cell line and per condition were transferred into the imaging plate (Cat. No. 6055300; PerkinElmer) – one organoid per well. Media leftovers were aspirated and 50 µl of CellTiter-Glo® reagent was added to each well. The plate was incubated for 30 min on a shaker at RT. Luminescence was measured using a Cytation5 M cell imaging reader. The experiment was repeated for five independent organoid generation rounds at day 30 and 60 of organoid generation. The luminescence readout per sample of each batch was normalised to the mean luminescence of the batch. A median of three organoids of each cell line and conditions was calculated and normalised to the size factor. The size factor for each cell line and condition was determined as a mean of random 20 organoids at day 30 and 10 organoids at day 60 from five independent organoid generation rounds. The area of organoids was measured using the Cytation5M cell imaging reader.

Fatty acid dependency assay (Seahorse XF Mito fuel flex test)

The rate of fatty acids oxidation was determined in 30 days old midbrain organoids following Seahorse XF Mito fuel flex test protocol (Agilent) and using Seahorse XFe96 Spheroid FluxPak (Cat. No. 102905-100; Agilent). The utility plate was coated with Corning® Cell-Tak™ Cell and Tissue Adhesive (Cat. No. 354241; Corning) and for 1 h incubated at 37°C before organoid seeding in the plate. Organoids were incubated for 1 h in Seahorse XF DMEM medium, pH 7.4 (Cat. No. 103575-100; Agilent) supplemented with 1 mM pyruvate, 2 mM glutamine, and 10 mM glucose at 37°C in the non-CO_2 incubator. The assay was performed for four independent organoid generation rounds, using 6–8 organoids per cell line and condition in each assay run. Results were normalised to the size factor. The size factor for day 30-old organoids for each cell line and condition was determined as a mean of random 20 organoids from the respective organoid generation rounds. The area of organoids was measured using the Cytation5M cell imaging reader. Data were analysed using the Seahorse Wave Desktop software (Agilent). Wells with aberrant oxygen consumption rate (OCR) patterns were excluded from each of the individual experiments.

Stable isotope tracing sample preparation

Cell culture media was prepared in DMEM w/o glucose (Cat. No. A1443001; Themor Fisher Scientific) and Neuobasal A w/o glucose (Cat. No. A2477501; Thermo Fisher Scientific). [U-^{13}C] glucose stable isotope tracer (Cat. No. CLM-1396; Eurisotop) was added to the media to a final concentration of 21.25 mM. Thirty days old, non-embedded organoids were incubated in the tracer medium for 24 h at 37°C, 5% CO_2 in a humidified incubator. Eight organoids per cell line and condition were pooled to perform metabolite extraction. Collected samples were first washed with 1× DPBS and then resuspended in 80 µl ice-cold extraction solvent (50% MeOH, 30% ACN, 20% H_2O). Samples were incubated in a thermo shaker at 4°C, 300 rpm for 5 min and then centrifuged at full speed at 4°C for 10 min. Seventy microliters of supernatant was transferred into LC-MS vials and stored at −80°C until the analysis.

LC-MS measurement

Metabolite analysis was performed using a Vanquish® Flex UHPLC system (Thermo Scientific) coupled to a Q Exactive® Plus Orbitrap® mass spectrometer (Thermo Scientific). Chromatography was carried out with a SeQuant® ZIC®-pHILIC 5 µm polymer 150 mm × 2.1 mm column (Merck AG) protected by a SeQuant® ZIC®-pHILIC Guard 20 mm × 2.1 mm pre-column. The temperature of the column was kept at 45°C and the flow rate was set to 0.2 ml/min. The mobile phases consisted of 20 mmol/l ammonium carbonate in water, pH 9.2 and supplemented with 5 µM of medronic acid (Eluent A) and Acetonitrile (Eluent B), loading and gradient occurs at 0.2 ml/min flow rate; loading step last 2 min with 80% B; then starts a linear gradient ranging from 80% B to 20% B in 15 min; at 18 min starts the regeneration step with 80% B; from 20 min until 24.5 min column is re-equilibrated with 80% B at flow rate of 0.4 ml/min. Five microliters of the sample were injected into the machine. The MS experiment was performed using electrospray ionisation with polarity switching enabled. Source parameters were applied as written here: sheath gas flow rate, 30; aux gas flow rate, 10; sweep gas flow rate, 0; spray voltage, 4 kV (+)/3.5 kV (−); capillary temperature, 350°C; S-lense RF level, 50; aux gas heater temperature, 100°C. The Orbitrap mass analyser was operated at a resolving power of 70,000 (at 200 *m*/*z*) in full-scan mode (scan range: *m*/*z* 75–1000; automatic gain control target set to 1e6 charges with a maximum injection time: 250 ms).

Data from LC-MS measurements were acquired with the Thermo Xcalibur software (v.4.3.73.11) and analysed using TraceFinder (v.4.1). Natural isotope abudance substraction and subsequent analysis was performed as previously described using in-house scripts.[30]

Reactive oxygen species detection with FACS

To quantitatively determine cytoplasmic reactive oxygen species (ROS) levels in live cells, 4–5 non-embedded organoids at day 30 of organoid culture were pooled per sample and dissociated using Accuatse (Cat. No. A6964; Sigma). Samples were first incubated with Accutase for 1 h at 37°C under dynamic conditions, following trituration with a 1000 or 200 µl pipette (depending on organoid size) to support organoid dissociation into single cells. Reducing incubation time to 30 min, these steps were repeated until organoids were fully dissociated. Each sample then was split into two 2 ml Eppendorf tubes as technical replicates for the assay. Samples were centrifuged for 3 min at 500 g and Accutase was replaced with 500 µl of assay medium containing 2 µM 2′,7′-dichlorofluorescein diacetate (DCFDA; Cat. No. D399; Thermo Fisher Scientific) and 1:1000 live-dead stain Zombie NIR (Cat. No. 423106; Biolegend) in DPBS (Cat. No. 14190250; Thermo Fisher Scientific). Cells were incubated with the assay media containing the fluorescent dyes for 20 min at 37°C. Samples were then run on BD LSRFortessa flow cytometer, acquiring 10,000 single-cell events (DCFDA+, live cells) per sample. Fluorescence intensity was analysed with FlowJo software (v.10.7.2). Data of two technical replicates per sample were averaged and the percentage of positive cells to the DCFDA staining was batch normalised to the mean percentage of the batch.

FACS-based glucose uptake assay using a 2-NBDG probe

Glucose uptake was measured using fluorescently tagged, non-metabolisable glucose analogue 2-(*N*-(7-nitrobenz-2-oxa-1,3-diazol-4-yl) amino)-2-deoxyglucose (2-NBDG; Cat. No. 11569116; Thermo Fisher Scientific). Samples were prepared as described in the section ‘Reactive oxygen species detection with FACS’. Cells were incubated for 30 min at 37°C with 1:500 2-NBDG and 1:1000 live-dead stain Zombie NIR (Cat. No. 423106; Biolegend) in cell culture media with either high or low insulin concentration. Samples were run on BD LSRFortessa flow cytometer, acquiring 10,000 single-cell events (2-NBDG+, live cells) per sample. Fluorescence intensity was analysed with FlowJo software (v.10.7.2). Data of two technical replicates per sample were averaged and the fluorescence intensity was batch normalised to the mean of IR condition.

Lipidomics

Lipidomics analysis was performed by Lipometrix (https://www.lipometrix.be) using HILIC LC-MS/MS. Samples were prepared as a pool of eight non-embedded organoids per cell and per condition from four independent organoid generation rounds. Samples were collected on day 30 of organoid culture, washed once with ice-cold PBS, snap-frozen in liquid nitrogen and stored at −80°C until the analysis. The concentration of detected lipid species was normalised to the DNA content of each sample.

Dopamine ELISA

Extracellular dopamine concentration was measured with Dopamine ELISA (Cat. No. BA-E-5300R; Immusmol) following the manufacturer's instructions. Dopamine ELISA was performed using a 750 µl volume of a sample. Each sample was a pool of 400 µl of supernatant from three embedded midbrain organoids, collected at day 60 of organoid culture, 72 h after the last media change. Samples were collected from three independent organoid generation rounds. Final dopamine concentration (nmol/l) was normalised to the mean nuclei count determined during the high-content imaging workflow from randomly selected three organoid sections per cell line and condition. Results were batch-corrected against the mean of each batch.

Data analysis and statistics

If not stated otherwise, data were analysed and visualised in GraphPad Prism (v.9.5.1) or R software (v.4.2.2). All data were batch-normalised for every experiment. Data normality was determined with the Shapiro-Wilk normality test. To determine the statistical significance of non-normally distributed data, we applied a two-tailed Wilcoxon signed rank test for paired samples and the Mann–Whitney *U*-test for experiments involving random samplings, such as imaging, local field potential recordings and multielectrode array. For normally distributed data, statistical significance was tested with a two-tailed, paired t-test with a degree of freedom n-1. The number of data points in each sample group for every experiment is provided in the figure legends. Significance asterisks represent $*p < 0.05$, $**p < 0.01$, $***p < 0.001$ (exact *p* values are provided in Table S4). Error bars represent mean + SD.

Results

Modification of cell culture media activates insulin signalling

Midbrain organoids were generated from three healthy individual iPSC-derived neuroepithelial stem cell lines (NESCs; Table S1) following a previously published protocol.[16–18] Before organoid generation, the quality of all NESC lines used in the study was confirmed by evaluating the expression of the stem cell marker SOX2, the neuronal progenitor marker Nestin and the neuroectoderm fate marker PAX6 (Figure S1). Midbrain organoids were cultured in two culture conditions that vary by the concentration of insulin (Figure 1(a)). First, we determined the insulin concentration in standard basal N2B27 media supplemented with insulin-containing neurotrophic supplements B27 and N2 used for the maintenance of NESCs and midbrain organoids. The insulin concentration in the standard basal media was 393.9 nM, which strongly exceeds the physiological insulin concentration in the central nervous system, reported to be below 0.1 nM (measured in cerebrospinal fluid).[31,32] We hypothesised that this supraphysiological insulin concentration in the standard media might cause insulin resistance (IR) in the organoid culture. We also measured insulin concentration in the supernatant of organoids cultured for 3 days in the standard media with the high insulin concentration and saw that the insulin concentration remained between 352 and 374 nM (Figure 1(b)). Next, to reduce insulin concentration in the media towards a more physiological one, we prepared a self-made N2 supplement following commercial N2 media formulation, only excluding insulin (see section 'Material and methods'). Insulin concentration in the N2B27 medium containing self-made N2 was 171.2 nM which is 2.3 times less than in the standard media. After 3 days of organoid culturing in this reduced insulin media, insulin concentration decreased even more, and was between 103.7 and 127.4 nM, suggesting increased usage of insulin by cells (Figure 1(b)). Further, we confirmed that self-made N2 supplement did not affect organoid development nor viability (Figure S2) and did not change cellular composition within organoids (Figure S3). Since dopaminergic neurons are the most relevant cell type for PD, we additionally validated the self-made N2 supplement on iPSC-derived dopaminergic neuron cultures. Self-made N2 media did not cause any changes in dopaminergic neuron differentiation capacity, determined by the similar levels of TH and TUJ1 markers in dopaminergic neurons cultured in standard and self-made N2 supplemented media (Figure S4A). To further confirm that a 2.3 times reduction of the insulin concentration is sufficient to change the activity of insulin signalling, we cultured midbrain organoids in these two insulin conditions from the start of organoid differentiation – day 2 of organoid culture and maintained until the sample collection – day 30 or 60 of organoid culture (Figure 1(a)).

We were able to demonstrate a significant reduction of insulin receptor substrate (IRS1) upstream insulin signalling in organoid samples cultured in the high insulin concentration standard media, confirming insulin signalling dysfunction in these organoids (Figure 1(c)). On the contrary, IRS1 was significantly more abundant in the organoid samples cultured in reduced insulin concentration media, suggesting that this condition promotes cellular

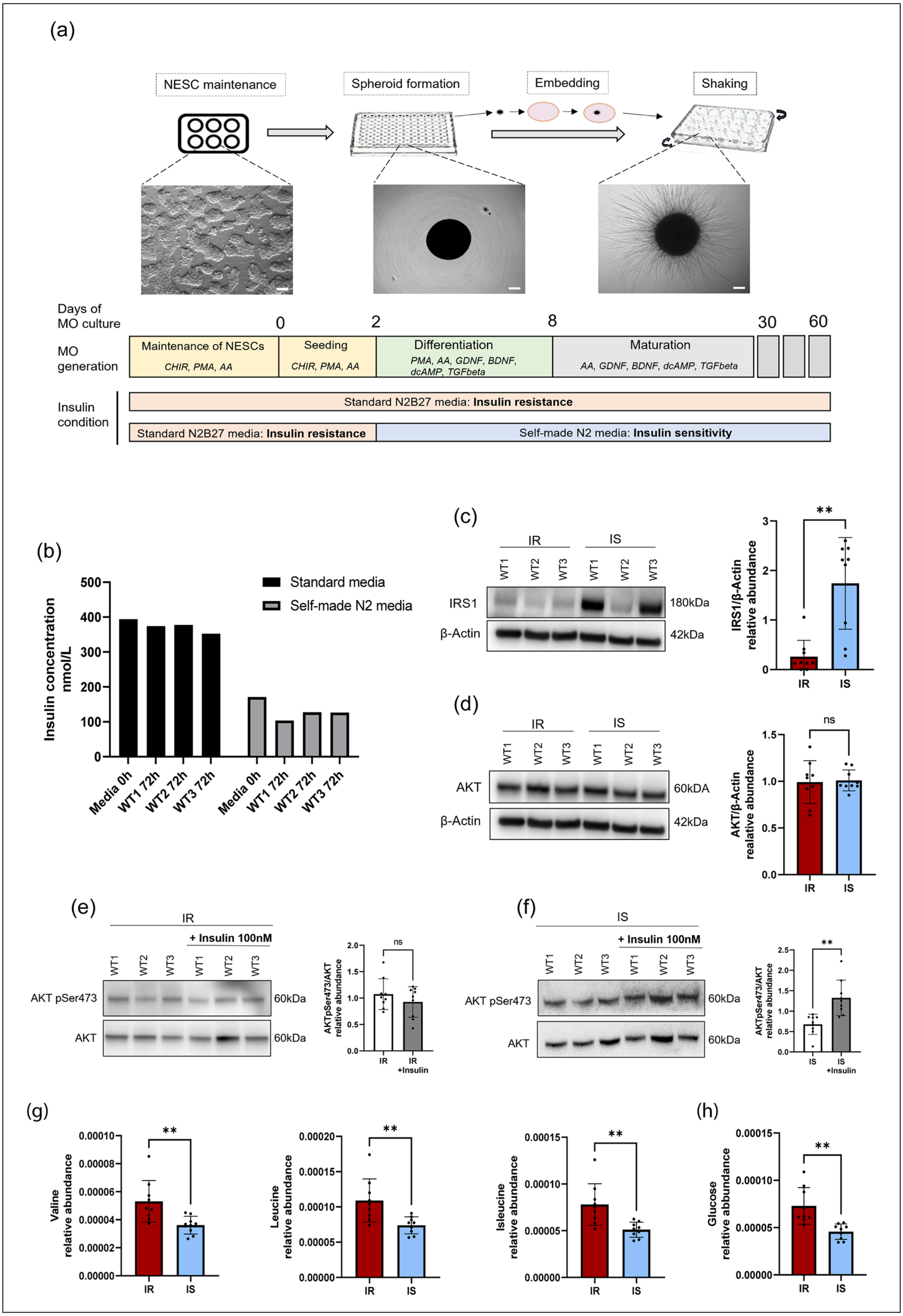

Figure 1. *(Continued)*

Figure 1. Modification of cell culture media activates insulin signalling: (a) representative image of midbrain organoid (MO) generation and cell culture media conditions. Scale bars 200 µm, (b) insulin concentration in standard media and self-made N2 media measured in fresh media (0 h) and after 3 days of incubation with cells (72 h), (c) representative image of WB and quantification of IRS1 levels relative to the housekeeping β-actin, (d) representative image of WB and quantification of AKT levels relative to the housekeeping β-actin, (e) representative image of WB and quantification of AKT pSer73 levels after acute stimulation with 100 nM of insulin in IR samples, relative to the total AKT levels, (f) representative image of WB and quantification of AKT pSer73 after acute stimulation with 100 nM of insulin in IS samples, relative to the total AKT levels. For panels (c)–(f) statistical significance was tested with the two-tailed, matched-pairs signed rank Wilcoxon test ($^*p < 0.05$, $^{**}p < 0.01$, $^{***}p < 0.001$). Error bars represent mean + SD. n (IR) = 9; n (IS) = 9. (g) Relative abundance of branched-chain amino acids – Valine, Leucine, and Isoleucine, detected by LC-MS in midbrain organoid supernatant after 72 h incubation with organoid, and (h) relative abundance of glucose, detected by LC-MS in midbrain organoid supernatant after 72 h incubation with organoid. For panels (g)–(h) statistical significance was determined with the two-tailed, paired *t*-test ($^*p < 0.05$, $^{**}p < 0.01$, $^{***}p < 0.001$). Error bars represent mean + SD. n (IR) = 9; n (IS) = 9.

insulin sensitivity (IS). Additionally, we looked at the abundance of the central protein of insulin signalling – AKT, which was not changed between organoids cultured in the two insulin conditions (Figure 1(d)). We triggered acute insulin signalling activation by organoid stimulation with 100 nM insulin for 2 h and observed that in response to insulin, there was an increase of AKT phosphorylation at Ser473 residue in IS organoids, while IR organoids did not show any change in AKT phosphorylation (Figure 1(e) and (f)), further demonstrating loss of insulin sensitivity. Similarly, the acute stimulation of only dopaminergic neurons with increasing concentrations of insulin was able to activate the insulin signalling pathway already at the dose of 10 nM, as indicated by the robust increase of AKT phosphorylation (both at Ser473 and Thr308 residues) in dopaminergic neurons cultured in self-made N2-based media. In contrast, even the highest dose of insulin (200 nM) was unable to increase phospho-AKT levels in dopaminergic neurons cultured in N2B27 media containing commercial N2, further supporting that insulin concentration change affects the insulin signalling also in dopaminergic neurons (Figure S4(b)).

To additionally confirm the IR and IS state of midbrain organoids cultured under different insulin concentration media, we measured levels of branched-chain amino acids which are considered biomarkers of insulin resistance and are found in higher levels in the plasma of individuals with changed metabolism and insulin resistance.[33,34] Accordingly, we saw their increased levels in IR organoid-conditioned media (Figure 1(g)). Furthermore, we observed that most of the metabolites present in the culture media were in significantly lower concentration in the IS organoid spent media after 3 days of incubation, indicating better metabolite uptake by IS organoids (Figure S5(a)). These metabolites included glucose, which was also found in significantly decreased levels in IS organoid spent media (Figure 1(h)). To verify increased glucose uptake by IS organoids, we treated dissociated organoids with a fluorescent glucose analogue 2-NBDG, to visualise glucose uptake by fluorescence-activated cell sorting (FACS; Figure S5(b)). We were able to observe a significantly increased fluorescent signal for IS organoids after acute insulin stimulation, further supporting that they are more insulin-responsive than IR organoids. To confirm that glucose uptake in midbrain organoids can be insulin-dependent, we investigated the glucose transporter (GLUT) presence in midbrain organoids. Along with the insulin-independent GLUTs, such as neuron-specific GLUT3 and glia-specific GLUT1, we were able to detect insulin-dependent GLUT4, which supports insulin's role in glucose uptake and regulation of metabolism in midbrain organoids (Figure S5(c)). Moreover, we observed that GLUT4 staining overlapped with the neuronal marker MAP2 (Figure S4(d)) and the glia marker GFAP (Figure S4(e)), suggesting GLUT4 expression in these cell types. Furthermore, we did not observe a significant difference in SOX2+ stem cells, MAP2+ neurons and the S100b+ glia population between IR and IS midbrain organoids at day 30 nor day 60 of organoid culture (Figure S3), hence we conclude that here presented metabolic differences are rather insulin concentration-dependent and not the consequence of changes in the cell type proportions within midbrain organoids.

Insulin sensitivity increases dopaminergic neuron amount and midbrain organoid functionality

After we confirmed that a reduced insulin concentration in the cell culture restores insulin signalling activity in the whole midbrain organoid as well as in the dopaminergic neurons, we wanted to assess whether insulin concentration affects dopaminergic neuron abundance. While at an earlier time point (day 30), there was no significant difference in the amount of TH-positive dopaminergic neurons between the two conditions, we observed a significantly higher number of dopaminergic neurons in IS midbrain organoids at day 60 of organoid culture (Figure 2(a) and (b)). Moreover, we confirmed that increased dopaminergic neuron amount in IS organoids is accompanied by a significant increase in dopamine production (Figure 2(c)). Considering the positive effect of insulin sensitivity on dopaminergic neuron levels and their ability to produce dopamine, we wanted to assess the role of insulin in the electrophysiological activity of the entire midbrain organoid. We measured spontaneous electrophysiological

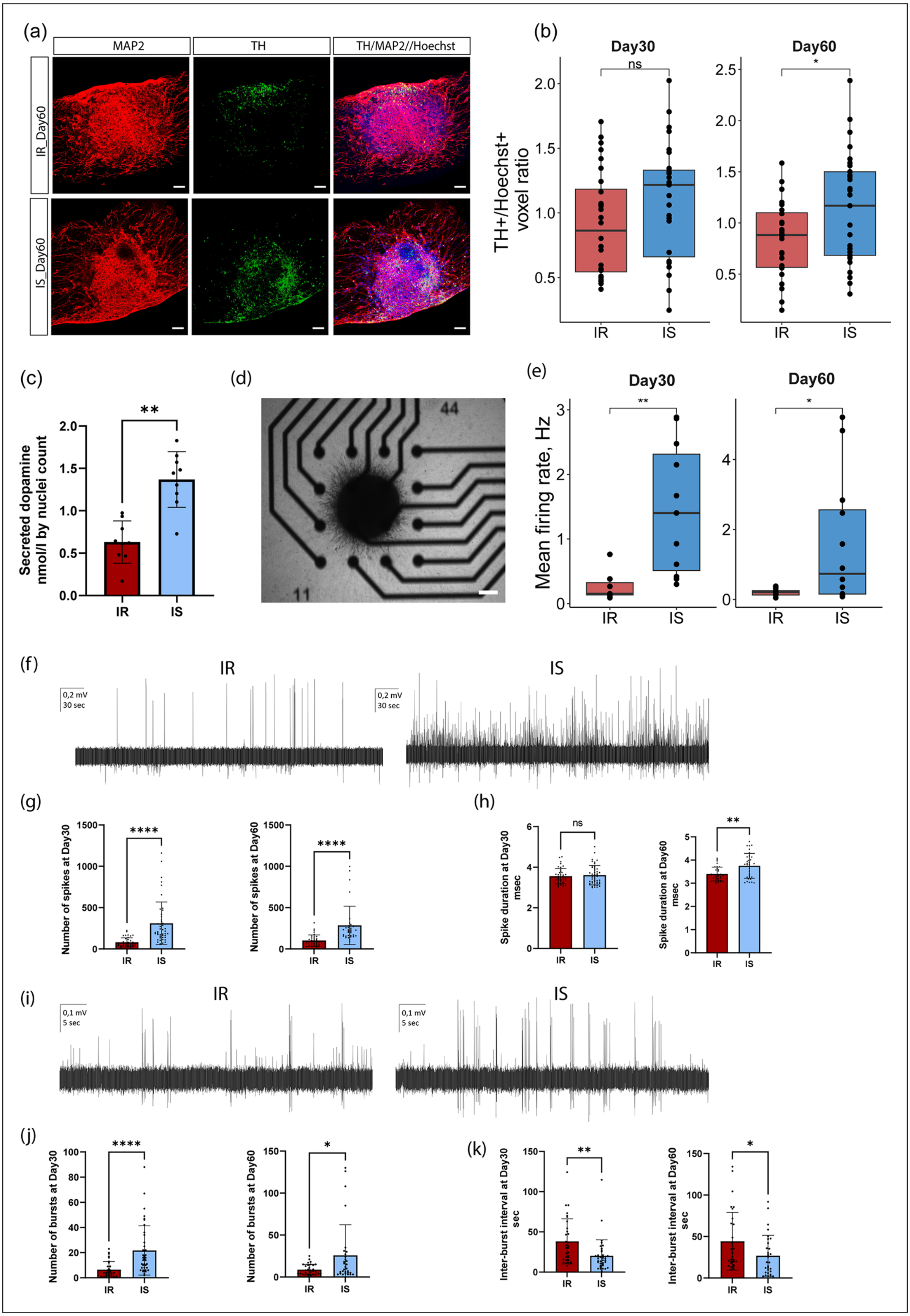

Figure 2. *(Continued)*

Figure 2. Insulin sensitivity increases dopaminergic neuron amount and midbrain organoid functionality: (a) Representative immunofluorescent images of TH and MAP2 staining in sections of 60 days old midbrain organoids. Scale bars 100 µm. (b) Quantification of TH positive area normalised to the Hoechst area in immunofluorescent stainings of 30 and 60 days old midbrain organoids. Statistical significance was tested with a two-tailed Mann–Whitney *U*-test (*$p < 0.05$, **$p < 0.01$, ***$p < 0.001$), *n* (IR Day 30) = 28; *n* (IS Day 30) = 27, *n* (IR Day 60) = 29; *n* (IS Day 60) = 29. (c) Extracellular dopamine levels measured in spent media of 60 days old midbrain organoids. Statistical significance was tested with the two-tailed, paired *t*-test (*$p < 0.05$, **$p < 0.01$, ***$p < 0.001$). Error bars represent mean + SD, *n* (IR) = 9; *n* (IS) = 9. (d) Representative image of an organoid placed on electrodes in a well of the multielectrode plate. Scale bar 200 µm. (e) Mean firing rate of 30 and 60 days old midbrain organoids. Recording time – 5 min. *n* (IR Day 30) = 7; *n* (IS Day 30) = 11, *n* (IR Day 60) = 9; *n* (IS Day 60) = 12. (f) Representative image of local field potential recording of spontaneous firing in midbrain organoids at day 30. (g) Quantification of spikes per time of recording (5 min) for day 30 and 60 old organoids. *n* (IR Day 30) = 40; *n* (IS Day 30) = 46), *n* (IR Day 60) = 34; *n* (IS Day 60) = 33. (h) Quantification of spike duration in seconds for day 30 and day 60 old organoids. *n* (IR Day 30); *n* (IS Day 30) = 46, *n* (IR Day 60) = 34; *n* (IS Day 60) = 33. (i) Representative image of local field potential recording of burst firing in midbrain organoids at day 60. (j) Quantification of bursts per time of recording (5 min) for day 30 and 60 old organoids. *n* (IR Day 30) = 32; *n* (IS Day 30) = 38, *n* (IR Day 60) = 31; *n* (IS Day60) = 30. (k) Quantification of inter-burst interval in seconds for day 30 and day 60 old organoids. *n* (IR Day 30) = 31; *n* (IS Day 30) = 38, *n* (IR Day 60) = 31; *n* (IS Day 60) = 30. For panels (g)–(k) statistical significance was tested with Mann–Whitney *U*-test (*$p < 0.05$, **$p < 0.01$, ***$p < 0.001$, ****$p < 0.0001$). Error bars represent mean + SD.

activity in the midbrain organoids using a multi-electrode array (MEA) system (Figure 2(d)) and observed that organoids cultured in IS conditions presented a significantly higher mean firing rate (Figure 2(e)). Furthermore, we confirmed the increased electrophysiological activity of IS organoids by recording local field potentials (LFP). Supporting the MEA data, IS organoids demonstrated a significantly higher number of spikes than IR organoids at both time points with an increased spike duration at day 60 of culture (Figure 2(f) and (h)). We were also able to detect bursts, which represent synchronised neuronal activity, occurring more often in IS organoids than in IR organoids again at both time points (Figure 2(i) and (k)), further confirming that insulin sensitivity promotes neuronal functionality.

Metabolic modelling predicts altered lipid metabolism and decreased glycolysis efficiency under insulin resistance

To further investigate metabolic alterations linked to insulin resistance, we performed metabolic modelling integrating RNA sequencing data of IR and IS midbrain organoids into the Recon3 human metabolic network.[26] Gene expression was integrated using the rFASTCORMICS pipeline,[27] which builds metabolic models based on gene discretisation (Figure S6(a)–(b)). We generated IR and IS models from pooled transcriptomic data between three cell lines cultured in the respective conditions. IR and IS model composition was not substantially different (Figure S6(c)). The IR model included 1446 genes, 3620 metabolic reactions and 2632 unique metabolites. While the IS model included 1430 genes, 3470 metabolic reactions and 2521 unique metabolites. Both models were primarily constrained by the N2B27 basis media composition, allowing uptake of only those metabolites that are present in the media. To capture differences in metabolism more accurately, we integrated major metabolic constraints such as glucose uptake and lactate production. We also added biomass constraint, as organoid growth between day 16 and 30 of culture to account for biomass change per unit of time, allowing more precise estimation of required metabolic rates of reactions present in the models.

By model composition analysis we identified the most different pathways by reaction composition between the two models (Figure 3(a)). The top metabolic pathways included several transport subsystems between cellular compartments and lipid metabolism-associated metabolic subsystems. To confirm that altered lipid metabolism is driven by insulin resistance, we validated our modelling results by performing lipidomic analysis, which detected an abundance of 18 different lipid classes in midbrain organoid samples. The lipid profile separated IR and IS samples in a principal component analysis (PCA) across the first principal component (11.6%), although the variance between the samples across the second component was higher (63.5%), demonstrating biological variability between the cell lines. We found that seven lipid classes were significantly differentially abundant between IR and IS samples (Figure S7). The most significantly dysregulated class and the major contributor to the IR sample separation were cholesterol esters (Figure 3(c) and (d)). Consistent with the *in silico* predicted alteration in glycerophospholipid metabolism, lipidomics analysis revealed that phosphatidylcholines, which are one of the most abundant cell membrane phospholipid classes, were significantly increased in IS samples (Figure 3(e)). Additionally, modelling predicted changes in arachidonic acid metabolism, therefore, we investigated lipid species across all measured lipid classes that contained arachidonic acid (C20:4) and its immediate precursor of eicosanoid family – eicosatrienoic acid (C20:3). We found 10 significantly differentially abundant species containing a 20-carbon backbone across six lipid classes, all being intermediates of glycerophospholipid metabolism, namely – triacylglycerides (TG),

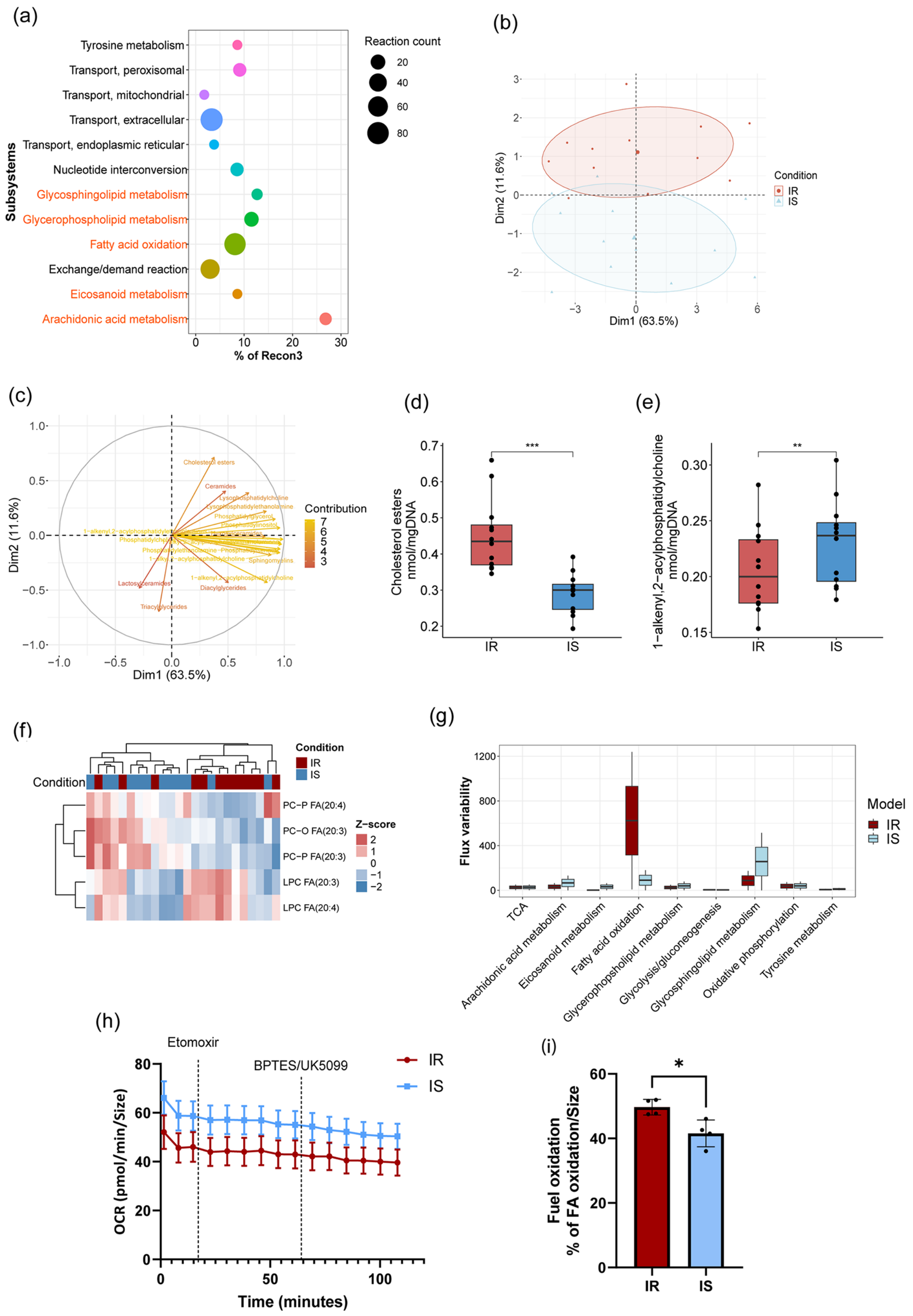

Figure 3. *(Continued)*

Figure 3. Insulin resistance-mediated lipid alterations. (a) Prediction of the most dysregulated metabolic pathways in the IR model based on model composition analysis. The size of a dot represents the number of reactions different between the two models. The location on the *x*-axis represents the percentage of reactions different from the total reaction number per subsystem in Recon3. Highlighted subsystems belong to lipid metabolism. (b) PCA scores plot of lipidomics analysis, demonstrating the percentage of variation between IR and IS sample lipidomic profiles, explained by the first and second components. (c) Correlation plot, demonstrating feature (individual lipid class) correlation across the samples and contribution to the variance between the conditions. (d) Quantification of Cholesterol esters. Concentration normalised to the mgDNA. (e) Quantification of 1-alkenyl,2-acylphospatidylcholine. Concentration normalised to the mgDNA. For panels (d)–(e) statistical significance was tested with the two-tailed, matched-pairs signed rank Wilcoxon test ($*p < 0.05$, $**p < 0.01$, $***p < 0.001$). *n* (IR) = 9; *n* (IS) = 9. (f) Unsupervised clustering of the most significantly differentially abundant lipid species derived from 20-carbon arachidonic or eicosatrienoic acid. (g) Prediction of metabolic pathway performance by flux variability analysis (FVA). (h) Fatty acid dependency measurements obtained using Seahorse assay. (i) Quantification of the percentage of fatty acid oxidation from the total fuel oxidation. Results normalised to the size of organoids. Statistical significance was tested using paired two-tailed *t*-test ($*p < 0.05$). Error bars represent mean + SD. *n* (IR) = 4; *n* (IS) = 4, representing the average value of independent experiments pooling data of individual cell lines.

phosphatidylcholine (PC), 1-alkyl,2-acylphosphatidylethanolamines (PC-O), 1-alkenyl,2-acylphosphatidylethanolamines (PC-P), lysophosphatidylcholine (LPC), lysophosphatidylethanolamine (LPE; Figure S8). Here the best separation between the IR and IS samples was achieved by major lipid components of the cellular membrane, including PC-Ps, PC-Os and the phosphatidylcholine*s* derivatives LPCs (Figure 3(f)). Altogether these results indicate that insulin resistance is inducing lipid changes that particularly affect cellular membrane and cholesterol metabolism.

Next, we carried out an *in silico* flux variability analysis (FVA) to predict the differences in metabolic performance of the subsystems of our interest. We included lipid subsystems with high differences in the composition between the models (Figure 3(a)), and central energy metabolism pathways – glycolysis, TCA and OXPHOS (Figure 3(g)). We observed higher flux flexibility in glycosphingolipid metabolism in the IS model compared to the IR model, suggesting that insulin resistance might impair glycosphingolipid metabolism. In contrast, the IR model showed much higher flexibility in fatty acid oxidation than the IS model, suggesting that fatty acid oxidation might contribute to energy generation in insulin-resistant conditions. We wanted to confirm this prediction by Seahorse metabolic assay, which allows us to evaluate organoid metabolic dependency on different carbon sources for energy generation. Indeed, we observed that IR organoids are about 10% more dependent on fatty acids than IS organoids (Figure 4(h) and (i)). We further performed *in silico* perturbations to determine the importance of glucose uptake and mitochondrial performance for the generation of ATP (Figure 4(a)). ATP levels were predicted to be slightly higher in the IS model compared to the IR model. We confirmed this by measuring intracellular ATP levels in 30 and 60 days old organoids, demonstrating significantly higher levels of ATP in IS samples at both time points (Figure 4(b) and (c)). There was no predicted difference in ATP generation by models after *in silico* blocking of mitochondrial complexes I and V. However, the prediction showed that the IS model is unable to generate ATP in case of glucose uptake obstruction (Figure 4(a)). This suggested that the IS model strongly relies on glucose to produce ATP. At the same time, the IR model showed an irrelevant change in ATP levels in case of blocking glucose uptake, implying possible usage of other carbon sources for energy generation under insulin resistance conditions. Additionally, we performed glucose C13 tracing to confirm increased glycolytic flux in IS samples. Indeed, we saw a significant increase in the relative labelled fraction of glycolytic intermediates directly derived from labelled glucose – 3-phosphoglycerate (3PG), phosphoenolpyruvate (PEP), pyruvate and lactate in IS samples (Figure 4(d)). However, tracing of labelled glucose did not reveal a labelling difference in TCA intermediates, suggesting no strong functional differences in mitochondrial metabolism between IR and IS midbrain organoids. In addition, we observed a higher relative labelled fraction of Ribose 5-phosphate and serine in the IS samples, compared to IR samples, pointing towards increased glucose-derived carbon distribution to the pentose-phosphate pathway and *de novo* serine synthesis respectively (Figure 4(e) and (f)). Further, we anticipated that altered metabolism in IR organoids might cause increased oxidative stress which plays an important role in the pathophysiology of PD. Accordingly, we detected significantly lower levels of NAD+/NADH ratio in IR samples, indicating an altered redox state of IR organoids. We also observed increased cytosolic ROS levels (Figure 4(h) and (i)), further confirming metabolic and redox disbalance in midbrain organoids driven by insulin resistance.

Discussion

In this study, we aimed to understand the molecular mechanisms through which T2D-associated insulin resistance might contribute to the onset and progression of PD. With a global prevalence of over 10% and a tendency to increase,[35,36] T2D has become a considerable risk factor for many diseases, including neurodegenerative disorders. Thus, there is a need to better understand T2D contribution to the onset and progression of these diseases. Moreover, PD is currently the fastest-growing neurodegenerative

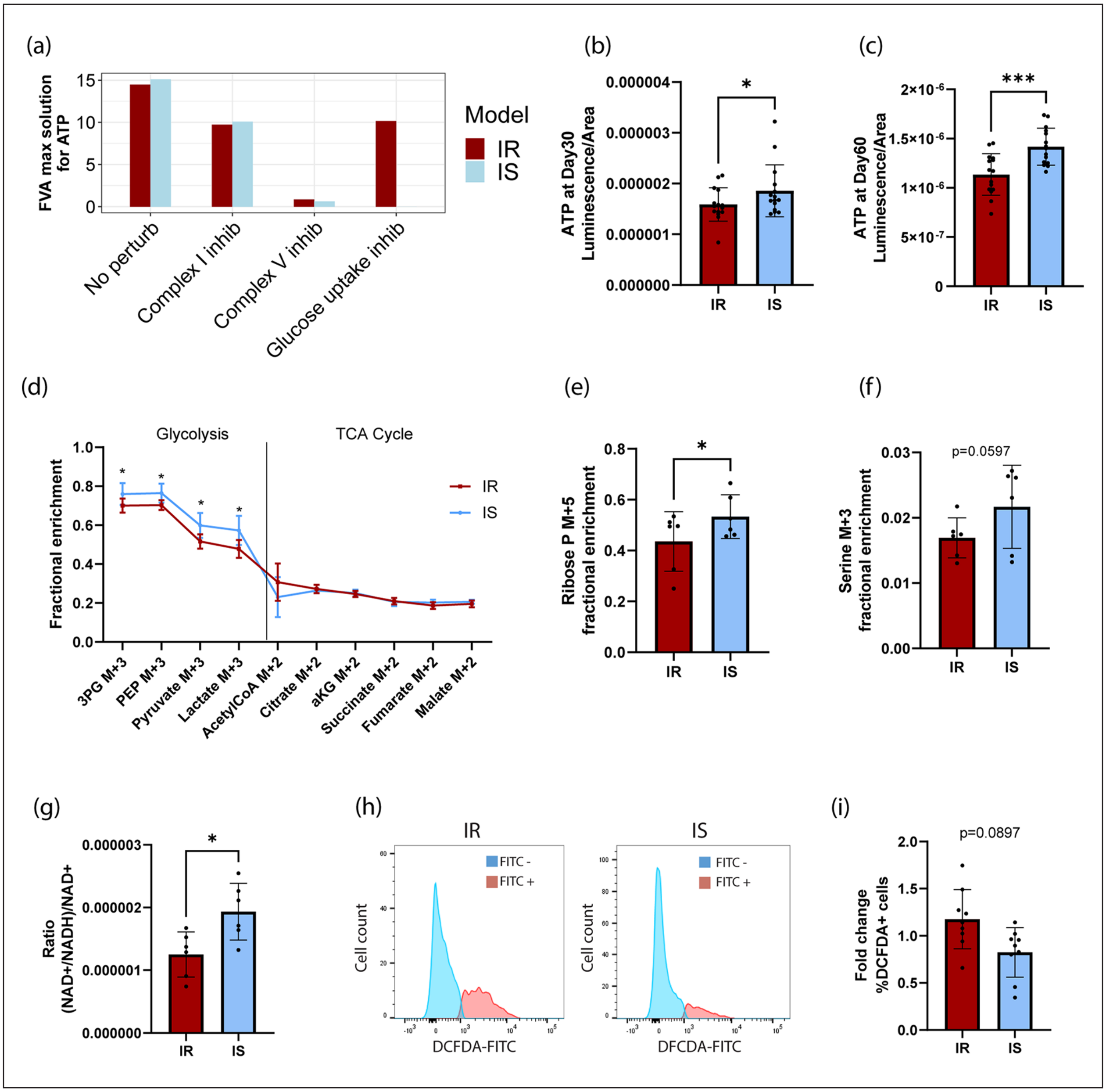

Figure 4. Insulin resistance compromises ATP levels and glycolysis efficiency: (a) Prediction of ATP production by IR and IS model following *in silico* inhibition of mitochondrial complexes present in the model and glucose uptake inhibition. (b) Intracellular ATP measurement for organoids at day 30 of organoid culture. n (IR) = 15; n (IS) = 15. (c) Intracellular ATP measurement for organoids at day 60 of organoid culture. n (IR) = 15; n (IS) = 15. (d) Fractional abundance of glycolysis and TCA metabolites derived from U^{13}C labelled glucose. n (IR) = 6; n (IS) = 6. (e) For panels (b)-(d) statistical significance was tested with the two-tailed, matched-pairs signed rank Wilcoxon test (*$p < 0.05$, **$p < 0.01$, ***$p < 0.001$). Error bars represent mean + SD. Quantification of Ribose 5-phosphate derived from U^{13}C labelled glucose. N (IR) = 6; n (IS) = 6. (f) Quantification of serine derived from U^{13}C labelled glucose. N (IR) = 6; n (IS) = 6. (g) The ratio of total and reduced NAD normalised to the total NAD levels. N (IR) = 6; n (IS) = 6. (h) Flow cytometry representative histograms, showing DCFDA positive (FITC-A+) fraction of cells in IR and IS condition. (i) Quantification of live cells positive to DCFDA (FITC-A) fluorescent signal. N (IR) = 9; n (IS) = 9. For panels (e)–(i) statistical significance was tested with the two-tailed, paired *t*-test (*$p < 0.05$, **$p < 0.01$, ***$p < 0.001$, ****$p < 0.0001$). Error bars represent mean + SD.

condition with still unclear molecular causes of neuronal death in the vast majority of cases.[37] Identification of risk factors might open new preventative strategies, halting the rising number of PD cases in future. Here, we show that insulin resistance, a hallmark of T2D, predisposes a healthy midbrain to PD-associated neurodegeneration by considerably altering metabolism and compromising the amount of dopaminergic neurons, which is the main affected neuronal type in PD.

However, investigating insulin signalling functional state *in vitro* is challenging due to the high amounts of insulin in the neurotrophic supplements, such as N2 and

B27, added to the culture media to promote neuronal differentiation and maturation. Insulin effects through the PI3K/AKT signalling pathway include regulation of cell proliferation, survival of progenitor cells, neuronal differentiation, synapse formation as well as the maintenance of energy homeostasis.[38–41] It has been demonstrated that human-origin neuronal cultures, including dopaminergic neurons, are particularly sensitive to insulin levels, with both insufficient and excessive insulin concentrations leading to neuronal death and growth defects.[40] Similar to our observation, Rhee et al. demonstrated optimal *in vitro* neuronal development around 200 nM of insulin, while higher concentrations showed insulin resistance phenotypes.[40] However, the optimal insulin concentration *in vitro* significantly exceeds insulin levels *in vitro*. An optimal insulin concentration in human plasma is around 5–15 mIU/l (0.03–0.09 nM),[31,42] reaching 80 mIU/l (0.56 nM) at hyperinsulinemic state.[43] The brain insulin concentration is estimated based on insulin levels in CSF, where normal insulin levels of healthy humans are around 1.6 mIU/l (0.01 nM),[31,44] increasing in response to elevated peripheral insulin levels.[31] Further studies are required to optimise insulin levels in the *in vitro* cultures to allow investigation of insulin effects on neurons at different developmental stages and in the disease context. In our study, the flexibility regarding insulin concentration was limited due to the confidentiality of ingredient concentrations in the B27 supplement. Thus, insulin concentration was only changed by the amount of insulin present in the N2 supplement. Importantly, the reduction of insulin achieved by replacing commercial N2 with self-made N2 without insulin, was sufficient to see differences in insulin signalling activity, allowing us to assess the effects of insulin resistance on midbrain organoids.

It has been previously reported that not only T2D but even pre-diabetes with insulin resistance as a common factor, promotes cognitive decline in PD patients.[7,45] We were able to demonstrate that under insulin resistance midbrain organoids display reduced spontaneous activity in the form of action potentials and bursts, suggesting decreased neuronal functionality, which could lead to cognitive impairment. Brain energetics is crucial in the coordination of electrophysiological activity[46,47] and since insulin signalling is a major regulator of metabolic processes, it is expected that insulin resistance would affect neuronal signal transmission. Although brain insulin sensitivity is controversial, mouse studies have shown that in some brain regions for rapid glucose uptake neurons are equipped with insulin-dependent glucose transporters in the proximity of synapses,[48,49] supporting insulin's role in controlling brain energy metabolism. Accordingly, we were able to show the presence of insulin-dependent GLUT4 along with the insulin-independent GLUT1 and GLUT3 transporters in midbrain organoids, suggesting at least partial insulin-dependent glucose uptake in the human midbrain. This also means that in the case of insulin resistance, neuronal functionality might be compromised due to insufficient glucose uptake for fast energy requirements A reduced glycolysis rate in IR organoids we also confirmed with glucose C13 tracing. However, we did not observe any changes in the levels of TCA intermediates derived from labelled glucose. This suggests that all glucose uptaken by cells in IR midbrain organoids is completely metabolised in the mitochondria for energy generation, probably to restore reduced levels of ATP. Moreover, we observed a slight but significant increase in fatty acid oxidation by IR organoids, which might present cell attempts to ensure sufficient energy levels in case of glucose unavailability. However, fatty acid oxidation is a considerable source of superoxide, which with time can exhaust anti-oxidative mechanisms and lead to cell damage.[50] At the same time, increased glucose uptake by IS organoids allows glucose usage for other metabolic pathways, such as *de novo* serine synthesis and nucleotide synthesis via the pentose-phosphate pathway. Both pathways are important for healthy brain function, playing a role in cell survival, neurotransmission, regulation of redox state, and lipid and protein synthesis.[51,52]

In addition, to the altered rate of fatty acid oxidation, we observed significant changes in abundance levels of several important lipid classes in IR midbrain organoids. Previous studies have reported elevated cholesterol ester levels associated with neurodegenerative diseases.[53–55] In line, we detected increased levels of cholesterol esters in IR organoids, suggesting that they undergo molecular changes linked to neurodegeneration. In addition, we demonstrated that most of the cellular membrane lipid classes containing arachidonic acid are differentially abundant between IR and IS midbrain organoids. Arachidonic acid is one the most abundant fatty acids in the brain and it has been associated with the prevention of α-Synuclein protein aggregation[56] and neuroprotection in animal models.[57] Moreover, it has been reported as a potential biomarker of PD,[58] suggesting its relevance in disease progression. Additionally, one of the most abundant cell membrane phospholipids – phosphatidylcholines were found to be significantly reduced in IR organoids, suggesting insulin resistance effect on cellular membrane integrity. Interestingly, metabolic modelling predicted changes in glycosphingolipid metabolism, which might play a role in phenotype acceleration in PD cases caused by a mutation in the GBA1 gene. Heterozygous mutation in the GBA1 gene has been identified in 5%–15% of all monogenic PD cases and is a major genetic risk factor for PD, associated with the accumulation of ceramides and glycosphingolipids – hexosylceramides, promoting PD pathophysiology.[59–61] Thus, altered glycosphingolipid metabolism might be an important link between the GBA1-associated PD and insulin resistance.

Human midbrain-specific organoids are known to comprise of various neuronal populations, including dopaminergic, glutamatergic, GABAergic, and serotonergic neurons.[62] We observed a significant reduction in the amount of dopaminergic neurons in midbrain organoids cultured under insulin-resistant conditions, suggesting their sensitivity to insulin-resistance-caused metabolic changes. While dopaminergic neurons are most affected in PD, non-dopaminergic neurons certainly also play an important role in the pathogenesis.[63] In our study, we examined insulin resistance-induced metabolic and electrophysiological changes across the entire midbrain organoid, without focusing on specific neuron types. Therefore, we cannot conclude which neuronal population is most impacted by insulin resistance. Nevertheless, the reduction in dopaminergic neuron number, along with decreased neuronal activity and altered metabolism, strongly indicate that insulin resistance predisposes healthy midbrain to PD development and might be a potential target in the prevention of neurodegeneration.

Acknowledgements

We would like to thank Prof. Dr. Rudi Balling for the valuable ideas that inspired this project. We acknowledge the support of the LCSB Bio-imaging Platform for high-content imaging and image analysis script optimisation, and assistance with flow cytometry experiments. RNA sequencing for RNA integration into metabolic models was performed at the LCSB Sequencing Platform. We would also like to extend our thanks to the metabolomics platforms at the LIH (particularly Laura Neises and Johannes Meiser) and the LCSB for conducting the metabolomics experiments, as well as the KU Leuven technology platform – Lipometrix for performing the lipidomics analysis.

Author contributions

A.Z. designed experiments, analysed and interpreted data, prepared figures, and wrote the original draft. J.K. analysed metabolic models. C.A. and A.V. carried out Western blot experiments. D.F. carried out the mounting of stained organoid sections. D.F. performed local field potential recordings and data analysis. G.A. and G.G.G. designed experiments, reviewed, and edited the manuscript. C.J. performed a GC-MS metabolomics experiment. P.A. supervised high-content imaging workflow. R.H. performed RNA sequencing. E.G. performed RNA sequencing data processing and preparation for metabolic modelling. E.S. supervised the metabolic modelling part, and reviewed, and edited the manuscript. J.C.S. conceived and supervised the project and edited the manuscript.

Availability of data

All data supporting the conclusions of this article are publicly available at: https://doi.org/10.17881/ztcz-2197

RNA sequencing data is available on Gene Expression Omnibus (GEO) under the accession code GSE237116.

Matlab and R scripts for data analysis and modelling are available on GitHub at: https://gitlab.com/uniluxembourg/lcsb/developmental-and-cellular-biology/zagare_2023_2

Declaration of conflicting interests

The author(s) declared the following potential conflicts of interest with respect to the research, authorship, and/or publication of this article: J.C.S. is a co-inventor on a patent covering the generation of the here-described midbrain organoids (WO2017060884A1). Furthermore, J.C.S. is a co-founder and shareholder of the company OrganoTherapeutics which makes use of midbrain organoid technology. G.G.G. is a lead scientist in OrganoTherapeutics. The other authors declare no competing interests.

Funding

The author(s) disclosed receipt of the following financial support for the research, authorship, and/or publication of this article: This work was mainly supported by the internal flagship project at the Luxembourg Centre for Systems Biomedicine and by the Luxembourg National Research Fund CORE grant to GA (C21/BM/15850547/PINK1-DiaPDs). Further, we acknowledge support from the National Centre of Excellence in Research on Parkinson's Disease (NCER-PD) which is funded by the Luxembourg National Research Fund (FNR/NCER13/BM/11264123).

Ethical approval

The work with iPSCs has been approved by the Ethics Review Panel (ERP) of the University of Luxembourg and the national Luxembourgish Research Ethics Committee (CNER, Comité National d'Ethique de Recherche). CNER No. 201901/01; ivPD

Informed consent

Not applicable.

Human rights

Not applicable.

Rights retention statement

This research was funded by the FNR-Luxembourg. For the purpose of Open Access, the author has applied a CC BY public copyright license to any Author Accepted Manuscript (AAM) version arising from this submission.

ORCID iD

Jens C Schwamborn https://orcid.org/0000-0003-4496-0559

Supplemental material

Supplemental material for this article is available online.

References

1. Ou Z, Pan J, Tang S, et al. Global trends in the incidence, prevalence, and years lived with disability of Parkinson's disease in 204 countries/territories from 1990 to 2019. *Front Public Health* 2021; 9: 776847.
2. Simon DK, Tanner CM and Brundin P. Parkinson disease epidemiology, pathology, genetics, and pathophysiology. *Clin Geriatr Med* 2020; 36: 1–12.
3. Yue X, Li H, Yan H, et al. Risk of Parkinson disease in diabetes mellitus: an updated meta-analysis of population-based cohort studies. *Medicine* 2016; 95: e3549.
4. De Pablo-Fernandez E, Goldacre R, Pakpoor J, et al. Association between diabetes and subsequent Parkinson

disease: a record-linkage cohort study. *Neurology* 2018; 91: e139–e142.

5. Cheong JLY, de Pablo-Fernandez E, Foltynie T, et al. The association between type 2 diabetes mellitus and Parkinson's disease. *J Parkinsons Dis* 2020; 10: 775–789.
6. Athauda D, Evans J, Wernick A, et al. The impact of type 2 diabetes in Parkinson's disease. *Mov Disord* 2022; 37: 1612–1623.
7. Park J, Choi S and Kim R. Association between prediabetes and cognitive function in Parkinson's disease. *Brain Behav* 2023; 13: e2838.
8. Barter JD, Thomas D, Ni L, et al. Parkinson's disease and diabetes mellitus: individual and combined effects on motor, cognitive, and psychosocial functions. *Healthcare* 2023; 11: 1316.
9. Bohnen NI, Kotagal V, Muller ML, et al. Diabetes mellitus is independently associated with more severe cognitive impairment in Parkinson disease. *Parkinsonism Relat Disord* 2014; 20: 1394–1398.
10. Labandeira CM, Fraga-Bau A, Arias Ron D, et al. Parkinson's disease and diabetes mellitus: common mechanisms and treatment repurposing. *Neural Regen Res* 2022; 17: 1652–1658.
11. Sabari SS, Balasubramani K, Iyer M, et al. Type 2 diabetes (T2DM) and Parkinson's disease (PD): a mechanistic approach. *Mol Neurobiol* 2023; 60(8): 4547–4573.
12. Knusel B, Michel PP, Schwaber JS, et al. Selective and nonselective stimulation of central cholinergic and dopaminergic development in vitro by nerve growth factor, basic fibroblast growth factor, epidermal growth factor, insulin and the insulin-like growth factors I and II. *J Neurosci* 1990; 10: 558–570.
13. Schulingkamp RJ, Pagano TC, Hung D, et al. Insulin receptors and insulin action in the brain: review and clinical implications. *Neurosci Biobehav Rev* 2000; 24: 855–872.
14. Hogg E, Athreya K, Basile C, et al. High prevalence of undiagnosed insulin resistance in non-diabetic subjects with Parkinson's disease. *J Parkinsons Dis* 2018; 8: 259–265.
15. Reinhardt P, Glatza M, Hemmer K, et al. Derivation and expansion using only small molecules of human neural progenitors for neurodegenerative disease modeling. *PLoS ONE* 2013; 8: e59252.
16. Monzel AS, Smits LM, Hemmer K, et al. Derivation of human midbrain-specific organoids from neuroepithelial stem cells. *Stem Cell Rep* 2017; 8: 1144–1154.
17. Nickels SL, Modamio J, Mendes-Pinheiro B, et al. Reproducible generation of human midbrain organoids for in vitro modeling of Parkinson's disease. *Stem Cell Res* 2020; 46: 101870.
18. Zagare A, Gobin M, Monzel AS, et al. A robust protocol for the generation of human midbrain organoids. *STAR Protoc* 2021; 2: 100524.
19. Harrison SE, Sozen B and Zernicka-Goetz M. In vitro generation of mouse polarized embryo-like structures from embryonic and trophoblast stem cells. *Nat Protoc* 2018; 13: 1586–1602.
20. Modamio J, Saraiva C, Giro GG, et al. Synaptic decline precedes dopaminergic neuronal loss in human midbrain organoids harboring a triplication of the SNCA gene. *BioRxiv*. Epub ahead of print 15 July 2021. DOI: 10.1101/2021.07.15.452499.
21. Hiller K, Hangebrauk J, Jager C, et al. MetaboliteDetector: comprehensive analysis tool for targeted and nontargeted GC/MS based metabolome analysis. *Anal Chem* 2009; 81: 3429–3439.
22. Bolognin S, Fossepre M, Qing X, et al. 3D cultures of Parkinson's disease-specific dopaminergic neurons for high content phenotyping and drug testing. *Adv Sci* 2019; 6: 1800927.
23. Monzel AS, Hemmer K, Kaoma T, et al. Machine learning-assisted neurotoxicity prediction in human midbrain organoids. *Parkinsonism Relat Disord* 2020; 75: 105–109.
24. Liao Y, Smyth GK and Shi W. The R package Rsubread is easier, faster, cheaper and better for alignment and quantification of RNA sequencing reads. *Nucleic Acids Res* 2019; 47: e47.
25. Yu G, Wang LG, Han Y, et al. ClusterProfiler: an R package for comparing biological themes among gene clusters. *OMICS* 2012; 16: 284–287.
26. Brunk E, Sahoo S, Zielinski DC, et al. Recon3D enables a three-dimensional view of gene variation in human metabolism. *Nat Biotechnol* 2018; 36: 272–281.
27. Pacheco MP, Bintener T, Ternes D, et al. Identifying and targeting cancer-specific metabolism with network-based drug target prediction. *EBioMedicine* 2019; 43: 98–106.
28. Heirendt L, Arreckx S, Pfau T, et al. Creation and analysis of biochemical constraint-based models using the COBRA Toolbox v.3.0. *Nat Protoc* 2019; 14: 639–702.
29. Norton WT, Abe T, Poduslo SE, et al. The lipid composition of isolated brain cells and axons. *J Neurosci Res* 1975; 1: 57–75.
30. Meiser J, Tumanov S, Maddocks O, et al. Serine one-carbon catabolism with formate overflow. *Sci Adv* 2016; 2: e1601273.
31. Wallum BJ, Taborsky GJ, Jr., Porte D, Jr., et al. Cerebrospinal fluid insulin levels increase during intravenous insulin infusions in man. *J Clin Endocrinol Metab* 1987; 64: 190–194.
32. Geijselaers SLC, Aalten P, Ramakers I, et al. Association of cerebrospinal fluid (CSF) insulin with cognitive performance and CSF biomarkers of Alzheimer's disease. *J Alzheimers Dis* 2018; 61: 309–320.
33. Newgard CB, An J, Bain JR, et al. A branched-chain amino acid-related metabolic signature that differentiates obese and lean humans and contributes to insulin resistance. *Cell Metab* 2009; 9: 311–326.
34. Batch BC, Shah SH, Newgard CB, et al. Branched chain amino acids are novel biomarkers for discrimination of metabolic wellness. *Metabolism* 2013; 62: 961–969.
35. Khan MAB, Hashim MJ, King JK, et al. Epidemiology of type 2 diabetes: global burden of disease and forecasted trends. *J Epidemiol Glob Health* 2020; 10: 107–111.
36. Sun H, Saeedi P, Karuranga S, et al. IDF diabetes Atlas: global, regional and country-level diabetes prevalence estimates for 2021 and projections for 2045. *Diabetes Res Clin Pract* 2022; 183: 109119.
37. Dorsey ER, Sherer T, Okun MS, et al. The emerging evidence of the parkinson pandemic. *J Parkinsons Dis* 2018; 8: S3–S8.

38. Réthelyi JM, Vincze K, Schall D, et al. The role of insulin/IGF1 signalling in neurodevelopmental and neuropsychiatric disorders: evidence from human neuronal cell models. *Neurosci Biobehav Rev* 2023; 153: 105330.
39. Chen W, Cai W, Hoover B, et al. Insulin action in the brain: cell types, circuits, and diseases. *Trends Neurosci* 2022; 45: 384–400.
40. Rhee YH, Choi M, Lee HS, et al. Insulin concentration is critical in culturing human neural stem cells and neurons. *Cell Death Dis* 2013; 4: e766.
41. Zhao Y, Xiao Z, Gao Y, et al. Insulin rescues ES cell-derived neural progenitor cells from apoptosis by differential regulation of Akt and ERK pathways. *Neurosci Lett* 2007; 429: 49–54.
42. Bolo NR, Jacobson AM, Musen G, et al. Hyperglycemia and hyperinsulinemia effects on anterior cingulate cortex myoinositol-relation to brain network functional connectivity in healthy adults. *J Neurophysiol* 2022; 127: 1426–1437.
43. Vaidya RA, Desai S, Moitra P, et al. Hyperinsulinemia: an early biomarker of metabolic dysfunction. *Front Clin Diabetes Healthc* 2023; 4: 1159664.
44. Gray SM, Meijer RI and Barrett EJ. Insulin regulates brain function, but how does it get there? *Diabetes* 2014; 63: 3992–3997.
45. McNay EC and Recknagel AK. Brain insulin signaling: a key component of cognitive processes and a potential basis for cognitive impairment in type 2 diabetes. *Neurobiol Learn Mem* 2011; 96: 432–442.
46. Capo Rangel G, Prezioso J, Gerardo-Giorda L, et al. Brain energetics plays a key role in the coordination of electrophysiology, metabolism and hemodynamics: evidence from an integrated computational model. *J Theor Biol* 2019; 478: 26–39.
47. Diaz-Garcia CM, Meyer DJ, Nathwani N, et al. The distinct roles of calcium in rapid control of neuronal glycolysis and the tricarboxylic acid cycle. *Elife* 2021; 10: e64821.
48. Ashrafi G, Wu Z, Farrell RJ, et al. GLUT4 mobilization supports energetic demands of active synapses. *Neuron* 2017; 93: 606–615.e603.
49. El Messari S, Leloup C, Quignon M, et al. Immunocytochemical localization of the insulin-responsive glucose transporter 4 (Glut4) in the rat central nervous system. *J Comp Neurol* 1998; 399: 492–512.
50. Schonfeld P and Reiser G. Why does brain metabolism not favor burning of fatty acids to provide energy? Reflections on disadvantages of the use of free fatty acids as fuel for brain. *J Cereb Blood Flow Metab* 2013; 33: 1493–1499.
51. Maugard M, Vigneron PA, Bolanos JP, et al. L-Serine links metabolism with neurotransmission. *Prog Neurobiol* 2021; 197: 101896.
52. Tu D, Gao Y, Yang R, et al. The pentose phosphate pathway regulates chronic neuroinflammation and dopaminergic neurodegeneration. *J Neuroinflammation* 2019; 16: 255.
53. Phillips GR, Hancock SE, Brown SHJ, et al. Cholesteryl ester levels are elevated in the caudate and putamen of Huntington's disease patients. *Sci Rep* 2020; 10: 20314.
54. van der Kant R, Langness VF, Herrera CM, et al. Cholesterol metabolism is a druggable axis that independently regulates tau and amyloid-beta in iPSC-derived Alzheimer's disease neurons. *Cell Stem Cell* 2019; 24: 363–375.e369.
55. Garcia-Sanz P, Orgaz L, Bueno-Gil G, et al. N370S-GBA1 mutation causes lysosomal cholesterol accumulation in Parkinson's disease. *Mov Disord* 2017; 32: 1409–1422.
56. Iljina M, Tosatto L, Choi ML, et al. Arachidonic acid mediates the formation of abundant alpha-helical multimers of alpha-synuclein. *Sci Rep* 2016; 6: 33928.
57. Qu Y, Zhang HL, Zhang XP, et al. Arachidonic acid attenuates brain damage in a rat model of ischemia/reperfusion by inhibiting inflammatory response and oxidative stress. *Hum Exp Toxicol* 2018; 37: 135–141.
58. Zhang J, Liu L, Zhang L, et al. Targeted fatty acid metabolomics to discover Parkinson's disease associated metabolic alteration. *J Mass Spectrom* 2021; 56: e4781.
59. Smith L and Schapira AHV. GBA variants and Parkinson disease: mechanisms and treatments. *Cells* 2022; 11: 1261.
60. Galvagnion C, Marlet FR, Cerri S, et al. Sphingolipid changes in Parkinson L444P GBA mutation fibroblasts promote alpha-synuclein aggregation. *Brain* 2022; 145: 1038–1051.
61. Navarro-Romero A, Fernandez-Gonzalez I, Riera J, et al. Lysosomal lipid alterations caused by glucocerebrosidase deficiency promote lysosomal dysfunction, chaperone-mediated-autophagy deficiency, and alpha-synuclein pathology. *NPJ Parkinsons Dis* 2022; 8: 126.
62. Smits LM, Magni S, Kinugawa K, et al. Single-cell transcriptomics reveals multiple neuronal cell types in human midbrain-specific organoids. *Cell Tissue Res* 2020; 382: 463–476.
63. Kalia LV, Brotchie JM and Fox SH. Novel nondopaminergic targets for motor features of Parkinson's disease: review of recent trials. *Mov Disord* 2013; 28: 131–144.